



Enhancement of photocatalytic activity and regeneration of Fe-doped TiO₂ (Ti_{1-x}Fe_xO₂) nanocrystalline particles synthesized using inexpensive TiO₂ precursor

Sudhakar Saroj¹ · Laxman Singh² · Rajiv Ranjan¹ · Satya Vir Singh¹

Received: 29 August 2018 / Accepted: 10 December 2018 / Published online: 5 January 2019
© Springer Nature B.V. 2019

Abstract

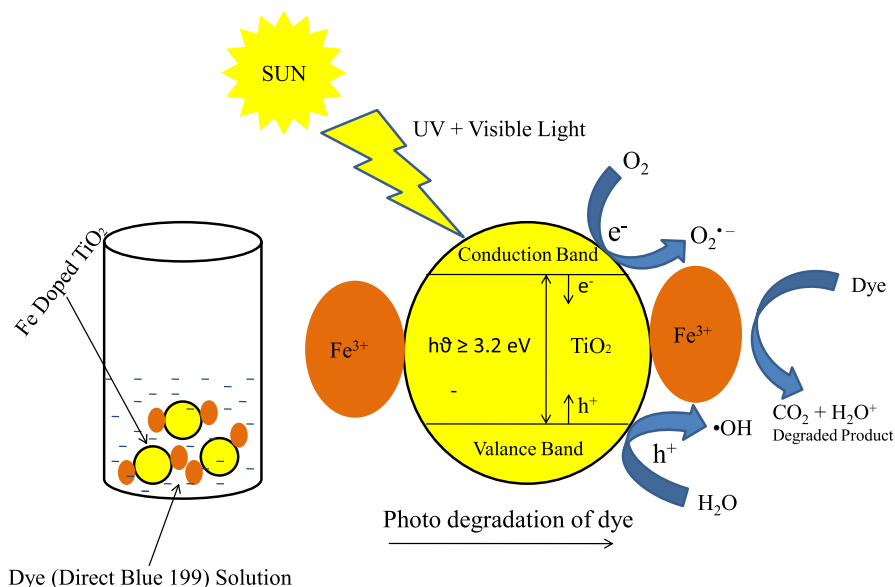
Fe-doped TiO₂, Ti_{1-x}Fe_xO₂ ($x = 0.00, 0.01, 0.03, 0.05, 0.07, \text{ and } 0.09$) photocatalysts with enhanced activity were synthesized via a citric-acid-assisted autocombustion method and characterized by X-ray diffraction (XRD) analysis, diffuse reflectance spectroscopy (DRS), Fourier-transform infrared (FTIR) spectroscopy, transmission electron microscopy (TEM), energy-dispersive X-ray spectroscopy (EDS), and X-ray photoelectron spectroscopy (XPS). The photocatalytic activity of the synthesized Fe-doped TiO₂ materials was evaluated using photodegradation of synthetic dye solution (Direct Blue 199) in photochemical and open pan reactors. Among the synthesized Fe-doped photocatalysts, Ti_{0.95}Fe_{0.05}O₂ showed the highest photodegradation activity. This Fe-doped TiO₂ photocatalyst was regenerated five times and its photocatalytic activity investigated.

✉ Satya Vir Singh
satyavirsingh59@rediffmail.com; svsinghche@itbhu.ac.in

¹ Department of Chemical Engineering, Indian Institute of Technology (BHU) Varanasi, Varanasi, U.P. 221005, India

² Department of Chemistry, R.R.S. College, Mokama, Patna, Bihar 803302, India

Graphical abstract



Keywords TiO_2 · Regeneration · Photocatalysts · Direct Blue 199

Introduction

Titanium dioxide (TiO_2) is an attractive and promising photocatalyst for decomposition of environmental pollutants, due to its high physicochemical stability, nontoxicity, and low cost [1, 2]. Titanium dioxide is used in production of pigments, paints, and cosmetics [3], as well as various other applications including gas sensors [4–7], sterilization or disinfection [8, 9], self-cleaning windows [10, 11], antireflection coatings for photovoltaic cells [12], photodegradation of organic pollutants in water and air, and catalytic oxidation of carbon monoxide [13–16].

Photocatalysts based on TiO_2 have been synthesized using various methods including sol–gel [17, 18], chemical vapor deposition [19, 20], hydrothermal [21, 22], and microemulsion [23, 24] techniques. The sol–gel method is reported to be an easy and appropriate method for synthesis of TiO_2 -based photocatalysts, since photocatalysts produced via this route exhibit high crystallinity, better quality and control of shape, etc.

In the TiO_2 -based photocatalytic process, electron–hole pairs are responsible for the photodegradation of any material, but poor interfacial charge transfer and rapid electron–hole recombination decrease the efficiency of TiO_2 photocatalysts. To enhance the photocatalytic activity of TiO_2 , many approaches have been tried in the recent past, including metal and nonmetal doping, formation of heterostructures,

etc. [25–31]. To inhibit electron–hole recombination, modification of TiO_2 with ions of metals such as Fe, Pd, Pt, Ag, Cu, W, and Hf has been investigated, since they can act as electron traps [32–34]. However, the concentration of such metal doping in the TiO_2 lattice must be optimal, because high metal ion concentrations in TiO_2 result in several types of centers for recombination of generated electron–hole pairs, suppressing the photocatalytic activity of TiO_2 [35–38].

The optimal concentration of dopants such as La, Mo, Ag, Fe, etc. in TiO_2 has been reported for photodegradation of various dyes such as Methylene Blue [39], Acid Yellow 29, Blue G 250, Acid Green 25 [41], and Rhodamine B [42] as well as 1,2-dichloroethane [40]. The cited studies show that the photocatalytic activity increases up to a certain doping percentage but declines thereafter.

In the present study, different concentrations of iron were doped into the TiO_2 lattice and the effect of the doping concentration on the photodegradation of Direct Blue 199 dye was studied. The synthesized photocatalysts were characterized using various physicochemical techniques such as XRD analysis, DRS, FTIR spectroscopy, EDS, and TEM. The characterization results showed that the activity of the synthesized photocatalysts strongly depended on the structure of the crystals, the particle size, the morphology of the photocatalyst, and its method of preparation. Photocatalytic processes for degradation of any pollutant in air or water become more economical if the applied photocatalyst can be regenerated. Therefore, one of the Fe-doped TiO_2 photocatalysts was regenerated and reused five times, and its photocatalytic activity studied in terms of the dye degradation kinetics. The performance of the synthesized undoped TiO_2 , $\text{Ti}_{0.95}\text{Fe}_{0.05}\text{O}_2$, and Aeroxide (Degussa) P-25 was compared for photodegradation of Direct Blue 199 dye.

Experimental

Chemicals

The chemicals used were titanium(IV) oxide (TiO_2 , 99%), ammonium sulfate GR $[(\text{NH}_4)_2\text{SO}_4]$, sulfuric acid (H_2SO_4 , 98%), citric acid monohydrate GR ($\text{C}_6\text{H}_8\text{O}_7 \cdot \text{H}_2\text{O}$), liquid ammonia with specific gravity of 0.91 (about 25% NH_3), nitric acid GR (HNO_3), and ferric oxide AR (Fe_2O_3). Direct Blue 199 dye was procured from the local market of Varanasi (India) and used to prepare dye solutions.

Preparation of Fe-doped TiO_2 photocatalysts

Nanocrystalline TiO_2 and Fe-doped TiO_2 photocatalysts ($\text{Ti}_{1-x}\text{Fe}_x\text{O}_2$ with $x = 1, 3, 5, 7,$ and 9 mol%) were synthesized using TiO_2 powder as precursor. The solution combustion technique was adopted in the synthesis of the Fe-doped TiO_2 nanoparticles. Titanium(IV) dioxide (TiO_2 , 0.063 mol) and ammonium sulfate $[(\text{NH}_4)_2\text{SO}_4$, 0.378 mol] were taken in 1:6 ratio and dissolved in 100 ml H_2SO_4 . The obtained mixture was heated with continuous stirring on a magnetic stirrer-cum-heater at 170°C and 400 rpm for 2–3 h to form titanium oxysulfate $[\text{TiO}(\text{SO}_4)]$. For 1 mol% Fe doping, 0.00031 mol ferric oxide was added in 100 ml sulfuric acid and heated

at 170 °C and 400 rpm for 1 h. This solution was added dropwise to titanium oxy-sulfate solution at the same temperature with continuous stirring. For the various other doping concentrations (3–9%), stoichiometric amounts of titanium and iron were taken as mentioned above. The content was made up to 500 ml. To this solution, 25% ammonium solution was added dropwise until neutralization. The precipitate was separated using a Büchner funnel and dissolved in 98% pure HNO₃. A stoichiometric amount of citric acid was dissolved in double-distilled water and mixed with the resultant mixture in a beaker. The whole content was then evaporated at 70–80 °C on a hot plate with continuous stirring until self-ignition. Ignition occurred at room temperature in an open environment, and burning proceeded by self-propagating combustion, exhausting a huge volume of gases and producing a dark-brown fluffy mass of Fe-doped TiO₂, which was ground using a pestle and mortar to produce Fe-doped TiO₂ powder. In the ignition step, citric acid acts as a complexing agent, creating a complex with cations and providing the fuel for combustion. At low temperature, the ignition step enhances the temperature to produce very fine crystalline powder [43]. The final Fe-doped TiO₂ photocatalysts were prepared after calcination of the obtained Fe-doped TiO₂ powders at 500 °C for 5 h.

Regeneration of used photocatalyst

To determine the photocatalytic activity of used photocatalyst, the degraded dye and photocatalyst after reaction were centrifuged. The separated solids were washed with distilled water then dried at 70 °C in a dryer and ground to obtain powder to determine the activity without regeneration.

To investigate the feasibility of the Ti_{1-x}Fe_xO₂ ($x=0.00-0.09$) photocatalysts for industrial applications, used Fe-doped TiO₂ photocatalyst (Ti_{0.95}Fe_{0.05}O₂) was regenerated and reused five times. The photocatalytic activity of the regenerated photocatalyst was examined by photodegradation of Direct Blue 199 dye in the photochemical reactor. Regeneration of the photocatalyst was carried out using the following procedure:

The whole content of degraded dye and photocatalyst was centrifuged for 20 min at 3500 rpm to separate the used photocatalyst from the entire solution. The photocatalyst settled to the bottom, while clear liquid rested on top. The liquid was sucked from the top with the help of a syringe, while the bottom solid which contained the used photocatalyst was washed with distilled water. The obtained material was poured into a glass Petri dish and dried in a dryer at 70 °C. The dried material was transferred to a crucible and calcinated at 500 °C for 5 h.

Characterization of synthesized TiO₂ photocatalysts

The phase constituents of the synthesized Ti_{1-x}Fe_xO₂ ($x=0.00-0.09$) photocatalysts were identified by XRD analysis using Cu K_α irradiation (Ultima IV; Rigaku, Japan), and the average crystallite size was determined from the XRD data using Scherrer's formula [44]. The binding energy of the elements in the samples were determined by XPS analysis (AMICUS, Kratos Analytical, UK) using a monochromated Mg K_α

(1253.6 eV) X-ray source. EDX and TEM analyses were carried out using a model 20 G² (Tecnai, FEI, USA) microscope. TEM was carried out to determine the crystal size and morphology of the synthesized Fe-doped TiO₂, with EDX for elemental analysis. The ultraviolet–visible (UV–Vis) absorption spectra of the synthesized Fe-doped TiO₂ photocatalysts were measured in the range of 200–700 nm by DRS (CORY 100 Bio UV spectrophotometer) with barium sulfate as internal standard. The indirect bandgap energy (E_g) of the Fe-doped TiO₂ photocatalysts was calculated using the Kubelka–Munk method by plotting $[F(R_\alpha)/hv]^{1/2}$ versus the photon energy (hv) [45].

The photocatalytic activity of all the synthesized photocatalysts was measured in terms of the degradation of Direct Blue 199 dye, measured based on the color concentration.

Photodegradation of Direct Blue 199 dye

The prepared Ti_{1-x}Fe_xO₂ ($x=0.00$ – 0.09) photocatalysts were used for photodegradation of Direct Blue 199 dye at four different concentrations (50, 100, 200, and 300 ppm) in aqueous solution.

For photodegradation of dye in a reactor, a UV photochemical reactor with eight ultraviolet tubes (wavelength 2537 Å) was used. The photochemical reactor and tubes (quartz and glass) were procured from Perfit India Ltd. Ambala (India). In the photochemical reactor, a quartz/glass tube was used to hold the dye solution, and the reactor also had a stirring facility. Aqueous dye solution (100 ml) was treated in a quartz or glass tube, because effective mixing of the dye solution and photocatalyst could only be achieved up to this solution volume.

Plastic tubs were used as open pan photochemical reactors (Fig. 1) with manual mixing every 5 min. Synthetic dye solution (1 l) was treated for 3 h in each batch. The height of the liquid (1 l) in the open pan reactor was 1 cm. The light intensity in

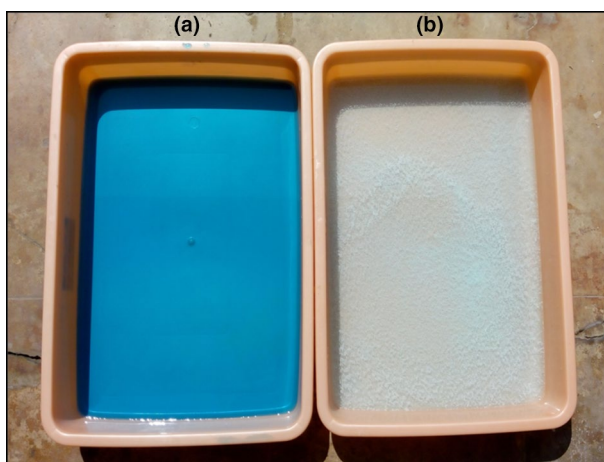


Fig. 1 Photodegradation of Direct Blue 199 dye in open pan reactor under sunlight over (a) undoped and (b) Ti_{0.95}Fe_{0.05}O₂ photocatalyst

Table 1 Intensity of solar radiation during photodegradation of Direct Blue 199 dye over undoped and Fe-doped TiO₂

Pyranometer report							
S. no.	Time	Direct solar radiation (W/m ²)	Diffuse solar radiation (W/m ²)	Air temp. (°C)	Air speed (m/s)	Wind direction (W-N)	RH (%)
<i>Date 01/05/2017</i>							
1	11:00	699	326	34.9	3.2	79	38
2	12:00	733	288	35.7	3.3	162	37
3	13:00	706	276	36	2.7	208	36
4	14:00	547	252	36.3	2.6	202	37
<i>Date 02/05/2017</i>							
1	11.00	841	177	38.7	0	48	22
2	12:00	819	185	39.4	2	132	22
3	13:00	749	233	40.1	0.4	57	20
4	14:00	605	212	40.3	1.6	104	22
<i>Date 03/05/2017</i>							
1	11:00	852	208	41.6	0.8	38	11
2	12:00	852	248	42.5	1.2	331	10
3	13:00	432	303	42.4	1.6	20	10
4	14:00	289	265	41.9	2.2	51	10
<i>Date 04/05/2017</i>							
1	11:00	553	340	39.7	2	55	25
2	12:00	776	268	40.1	3.3	176	24
3	13:00	675	253	41	1	131	24
4	14:00	552	275	41.7	2.3	159	17
<i>Date 05/05/2017</i>							
1	11:00	862	222	41.4	3	38	17
2	12:00	828	237	42.1	2.8	350	18
3	13:00	734	251	42.8	2.4	57	10
4	14:00	630	234	43.2	4.3	39	10
<i>Date 06/05/2017</i>							
1	11:00	823	235	43.2	1.4	78	10
2	12:00	814	235	43.8	0.8	337	10
3	13:00	759	234	43.9	1.4	103	10
4	14:00	533	248	44.5	1.8	132	10
<i>Date 08/05/2017</i>							
1	11:00	797	245	38.6	1.9	104	37
2	12:00	769	257	39.2	1.5	198	35
3	13:00	669	273	41.5	0.7	301	35
4	14:00	394	266	41.1	0.8	145	31
<i>Date 09/05/2017</i>							
1	11:00	346	322	34.9	0.3	259	42
2	12:00	562	464	36.5	0.5	170	41
3	13:00	331	558	36.9	2.2	181	35

Table 1 (continued)

Pyranometer report							
S. no.	Time	Direct solar radiation (W/m ²)	Diffuse solar radiation (W/m ²)	Air temp. (°C)	Air speed (m/s)	Wind direction (W–N)	RH (%)
4	14:00	264	299	37	0.6	203	36
<i>Date 10/05/2017</i>							
1	11:00	785	225	36.4	1.4	174	43
2	12:00	773	234	38.1	2.1	237	40
3	13:00	684	223	39.9	0.9	265	32
4	14:00	589	228	40.2	0.8	238	29
<i>Date 11/05/2017</i>							
1	11:00	782	243	37	1.6	279	53
2	12:00	769	250	37.9	2	112	51
3	13:00	691	297	39.3	1.8	205	41
4	14:00	600	348	40.5	1.9	138	35

the photochemical reactor is greater compared with sunlight, so the treatment duration of each batch was set as 1 h in the photochemical reactor versus 3 h in the open pan reactor.

Photodegradation of dye under sunlight is significantly affected by solar radiation, diffuse solar radiation, air temperature, air speed, and relative humidity, thus all of these factors were recorded continuously with the help of a pyranometer during the experiments from 11:00 AM to 2:00 PM. Table 1 presents the variation of the solar radiation with time.

The dye may be degraded under sunlight or a UV light source in the absence of photocatalyst, and may also adsorb on the photocatalysts. Therefore, two separate studies were performed to determine the contribution of these two effects to the color reduction, as follows:

To determine the adsorption of the dye on the Fe-doped TiO₂ photocatalysts, 100 ml of each dye solution (50, 100, 200, and 300 ppm) was taken in four glass tubes of the reactor, and 0.01 g Fe-doped TiO₂ photocatalyst was added to each tube, which was wrapped with black paper sheet and kept in the photochemical reactor for 1 h. In this study, the UV light of the photochemical reactor was kept off, but stirring was applied for 1 h. Samples of 1 ml were withdrawn from each of the tubes every 10 min, and their color concentration was analyzed.

To determine the photodegradation of the dye under sunlight in the absence of photocatalyst, 1 l of each dye solution (50, 100, 200, and 300 ppm) was taken in an open pan reactor and kept under sunlight for 3 h. Samples of 1 ml were withdrawn from the pan every 10 min, and their color concentration was analyzed. To determine the photodegradation of the dye in the absence of photocatalyst under UV light, the photochemical reactor was used. Solution (100 ml) was taken in a quartz tube with continuous stirring, samples of 1 ml were drawn at intervals of 10 min, and their color concentration was analyzed.

The photocatalytic activity of regenerated Fe-doped TiO₂ photocatalyst was determined in the photochemical reactor with quartz tube only. The same experimental procedure was followed as mentioned above. In this study, only regeneration of the 5% Fe-doped TiO₂ photocatalyst was studied, since it showed the best photocatalytic activity (fastest dye degradation) among all the synthesized photocatalysts, as seen in Fig. 8.

The actual reduction of the dye in solution due to photodegradation over the undoped and Fe-doped TiO₂ photocatalysts was calculated by subtracting the reduction in color due to adsorption on the photocatalyst plus the loss of dye in the blank dye solution (without any photocatalyst) from the total color reduction at each time.

The dye concentration was determined by UV–Vis spectrophotometry at wavelength of 594 nm. The percentage photocatalytic decomposition of Direct Blue 199 dye was determined using Eq. (1).

$$\% \text{ change in concentration due to photodegradation} = \frac{(C_0 - C_f) - C_{ad} - C_b}{C_0 - C_{ad}} \times 100, \quad (1)$$

where C_0 and C_f are the initial and final concentration of dye, and C_{ad} and C_b are the concentration change due to adsorption and loss of dye in blank solution (under similar experimental conditions), respectively.

The dye degradation kinetics in the photochemical reactor was studied using glass and quartz tubes. Experiments were performed with four concentrations of aqueous dye solution (50, 100, 200, and 300 ppm). A total of eight experiments, four with glass tube and four with quartz tube, were performed with one catalyst. In each experiment, 100 ml dye solution was taken in a glass/quartz tube, 0.01 g Fe-doped TiO₂ photocatalyst was added, and a magnetic bar was put into it. The UV lamp was switched on along with the stirrer. Samples of 2 ml were withdrawn from the tube at intervals of 5 min for 1 h, and their color content was analyzed after centrifugation. The dye degradation kinetics of all the synthetic aqueous dye solutions over different undoped and Fe-doped TiO₂ photocatalysts was studied using this method in the photochemical reactor in both glass and quartz tubes.

To study the dye degradation kinetics under sunlight, 1 l aqueous solution of synthetic dye sample was taken in an open pan reactor and 0.1 g undoped or Fe-doped TiO₂ photocatalyst was added, followed by manual mixing and exposure to sunlight. Samples of 2 ml were withdrawn at intervals of 5 min, and their color concentration was analyzed after centrifugation. The kinetic experiments were carried out at the four concentrations (50, 100, 200, and 300 ppm) of aqueous dye solution with all the undoped and Fe-doped TiO₂ photocatalysts.

The degradation kinetics of the synthetic aqueous dye solutions was studied at all four concentrations (50, 100, 200, and 300 ppm) over the undoped TiO₂ and 1–9% Fe-doped TiO₂ photocatalysts, with both light sources (UV light in the photochemical reactor with both glass and quartz tubes, and sunlight in the open pan reactor). For better understating of the kinetics, the photodegradation experiments are divided into 18 systems as follows: in the photochemical reactor with the glass tube with undoped TiO₂ photocatalyst (system 1), Ti_{0.99}Fe_{0.01}O₂ catalyst (system 2), Ti_{0.97}Fe_{0.03}O₂ catalyst (system 3), Ti_{0.95}Fe_{0.05}O₂ (system 4), Ti_{0.93}Fe_{0.07}O₂ catalyst

(system 5), and $\text{Ti}_{0.91}\text{Fe}_{0.09}\text{O}_2$ catalyst (system 6); in the photochemical reactor with the quartz tube with undoped TiO_2 photocatalyst (system 7), $\text{Ti}_{0.99}\text{Fe}_{0.01}\text{O}_2$ catalyst (system 8), $\text{Ti}_{0.97}\text{Fe}_{0.03}\text{O}_2$ catalyst (system 9), $\text{Ti}_{0.95}\text{Fe}_{0.05}\text{O}_2$ catalyst (system 10), $\text{Ti}_{0.93}\text{Fe}_{0.07}\text{O}_2$ catalyst (system 11), and $\text{Ti}_{0.91}\text{Fe}_{0.09}\text{O}_2$ catalyst (system 12); and in the open pan reactor under sunlight with undoped TiO_2 photocatalyst (system 13), $\text{Ti}_{0.99}\text{Fe}_{0.01}\text{O}_2$ catalyst (system 14), $\text{Ti}_{0.97}\text{Fe}_{0.03}\text{O}_2$ catalyst (system 15), $\text{Ti}_{0.95}\text{Fe}_{0.05}\text{O}_2$ catalyst (system 16), $\text{Ti}_{0.93}\text{Fe}_{0.07}\text{O}_2$ catalyst (system 17), and $\text{Ti}_{0.91}\text{Fe}_{0.09}\text{O}_2$ catalyst (system 18).

The photocatalytic activity of fresh and regenerated $\text{Ti}_{0.95}\text{Fe}_{0.05}\text{O}_2$ TiO_2 photocatalyst in terms of the dye degradation kinetics was studied based on kinetic experiments carried out as discussed above, at dye concentration of 200 ppm in aqueous solution in the photochemical reactor with the quartz tube.

A comparative study of the prepared undoped TiO_2 and the best doped material, i.e., $\text{Ti}_{0.95}\text{Fe}_{0.05}\text{O}_2$, and Aeroxide P-25 (supplied by Sigma Aldrich) was carried out by photodegradation of 200 ppm dye solution in the photochemical reactor with the quartz tube under the same experimental conditions as discussed above.

Results and discussion

Characterization of photocatalysts

XRD analysis

To elucidate the crystal structure and phase constituents of the various undoped and Fe-doped TiO_2 photocatalysts, XRD analysis was performed (Fig. 2a). The XRD profiles revealed only anatase phase for all the photocatalysts, corresponding to Joint Committee on Powder Diffraction Standards (JCPDS) card no. 21-1272. The absence of peaks corresponding to iron or its compounds in the XRD profiles for any level of doping indicates that iron oxide did not form on the TiO_2 surface; rather Fe^{3+} ions were successfully incorporated into the TiO_2 lattice due to the similar ionic radii of Ti^{4+} (0.68 Å) and Fe^{3+} (0.64 Å). Such incorporation of Fe^{3+} ions into the TiO_2 lattice was also reported previously [46]. A small shift of the (101) peak towards higher 2θ value, corresponding to a decreasing trend in the interplanar spacing, was also observed with increasing Fe concentration in the TiO_2 . Ion substitution (Fe^{3+} for Ti^{4+}) is the main cause of this peak shift and interplanar spacing reduction, since substitution of Fe^{3+} for Ti^{4+} creates oxygen vacancies (to maintain charge neutrality), which will reduce the interplanar spacing and thus increase the 2θ value. This pattern of peak shifting is supported by earlier work [47]. The average particle size of the synthesized photocatalysts with 0–9% doping ranged from 29.2 to 22.5 nm, as determined using Scherrer's formula [44] (Fig. 2b, inset). It is generally believed that the crystallinity of a sample depends on the intensity of the diffraction peaks. As shown in Fig. 2b, the undoped TiO_2 photocatalyst showed the highest peak intensity, whereas the peak intensity decreased with increasing Fe doping concentration in TiO_2 . This result indicates that presence of Fe^{3+} ions in the TiO_2 photocatalyst decreased its crystallinity, similar to previous work [48]. From the inset of

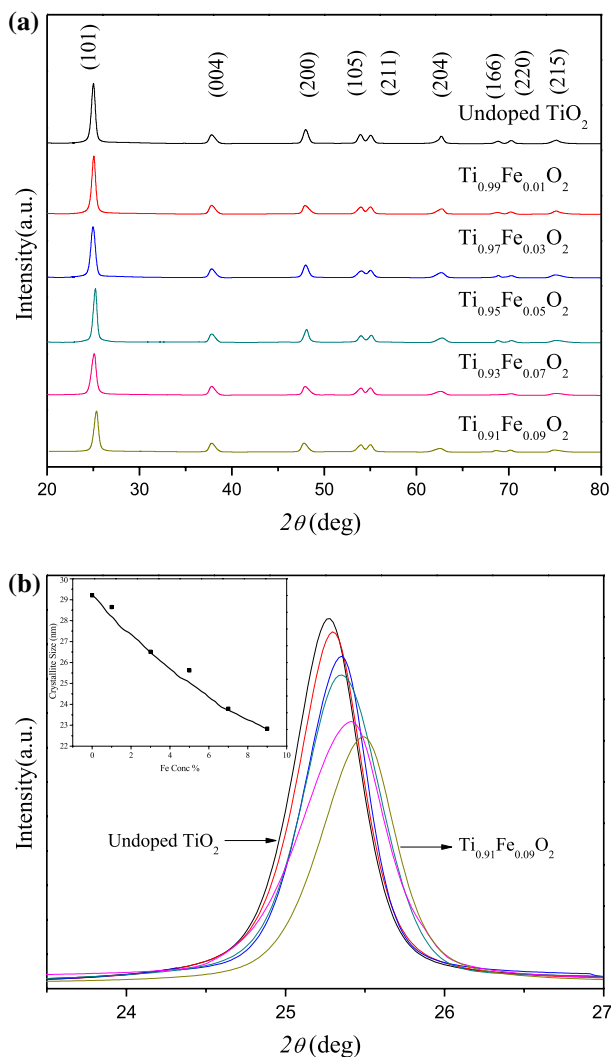


Fig. 2 **a** XRD patterns of undoped and (1–9%) Fe-doped TiO₂ photocatalysts. **b** Variation of the intensity of the (101) peak and shift of the angle with doping. Inset: effect of the Fe concentration on the crystallite size

Fig. 2b, it is visible that, with increasing doping concentration, the crystallite size of the photocatalysts decreased. Such decrease in crystallite size on Fe doping was also reported previously [49, 50]. During heat treatment, the crystal growth of Fe-doped TiO₂ photocatalyst is restricted by substitution of Fe³⁺ for Ti⁴⁺ due to lattice distortion in TiO₂ [48], and additives to TiO₂ can also obstruct contact between photocatalyst particles [49].

DRS

DRS analysis of the undoped and Fe-doped TiO₂ photocatalysts was carried out to determine their bandgap energy (Fig. 3). The spectra of the undoped and Fe-doped TiO₂ materials were recorded in the range of 200–800 nm (Fig. 3, inset a), revealing that Fe doping of TiO₂ shifted the absorption band toward the visible region. Based on the absorbance versus wavelength data, the indirect bandgap energy of the undoped TiO₂ and Fe-doped TiO₂ photocatalysts was determined using plots of $[F(R_\alpha)hv]^{1/2}$ versus $h\nu$ (Fig. 3), where $F(R_\alpha)$ is known as the Kubelka–Munk function and can be expressed as

$$F(R_\alpha) = (1 - R_\alpha)^2 / 2R_\alpha, \tag{2}$$

where $R_\alpha = 10^{-A}$ is the reflectance coefficient of the sample calculated from the absorbance A .

The bandgap energy of the Fe-doped TiO₂ photocatalysts narrowed with increasing Fe concentration (Fig. 3, inset b). The bandgap of the prepared nanoparticles narrowed from 3.19 to 2.47 eV (for the Ti_{0.95}Fe_{0.05}O₂ catalyst). Such bandgap reduction was also reported previously on iron doping of TiO₂ [48]. A significant shift of the absorption band from the UV to visible region is also achieved on doping TiO₂ with ions of other metals such as V, Cr, Mn, Co, Ni, Cu, etc. [51–54]. Transfer of electrons from Fe 3d orbitals to the conduction band of TiO₂ is the main cause of this bandgap shift. Fe³⁺ doping of TiO₂ introduces novel energy levels (Fe³⁺/Fe⁴⁺) without modifying the position of the edge of the valence band of TiO₂, thereby

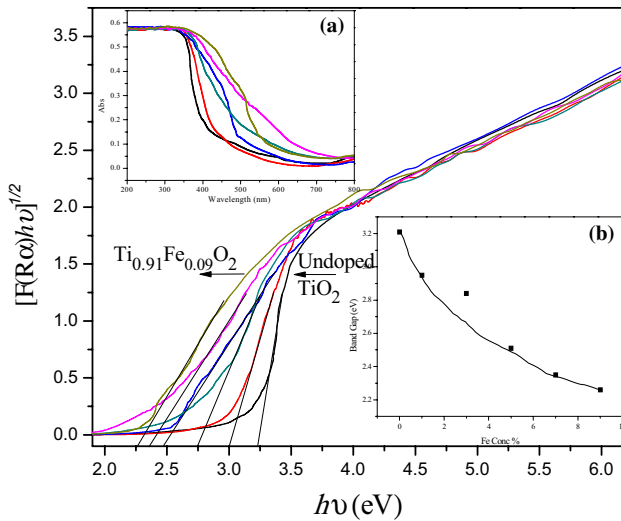


Fig. 3 Plots of $[F(R_\alpha)hv]^{1/2}$ versus photon energy. Insets: (a) UV–Vis diffuse spectrum, (b) variation of bandgap energy with Fe concentration

facilitating electron transfer from the Fe energy level ($\text{Fe}^{3+}/\text{Fe}^{4+}$) to the conduction band of TiO_2 . The color of the photocatalysts changed from white to yellow with increase of the percentage Fe doping in TiO_2 , similar to previous study [55].

FTIR spectroscopy

The FTIR spectra of the undoped and Fe-doped TiO_2 photocatalysts are shown in Fig. 4, revealing various vibrational bands. The weak absorbance bands in the ranges from 3400 to 3150 and 1650 to 1450 cm^{-1} correspond to stretching vibration of O-H^- groups and bending vibration of adsorbed water molecules, respectively, indicating coordination vacancies in the presence of water. Stretching and bending vibrations of O-H^- occur in a similar range [56, 57]. The photocatalytic activity of the synthesized Fe-doped TiO_2 nanoparticles may increase due to the presence of hydroxyl group (OH^-), since it can serve as the main scavenger of photogenerated charge carriers, leading to formation of the hydroxyl radical (OH^\cdot) required for dye degradation [39]. In Fig. 4, the transmittance band lies between 840 and 630 cm^{-1} , revealing that Ti-O-Ti stretching plays an important role in enhancing the photocatalytic activity of the Fe-doped TiO_2 photocatalysts. TiO_2 in anatase phase shows strong FTIR absorption bands in the region from 850 to 650 cm^{-1} [58].

XPS

The binding energy and chemical states of the elements (Ti, O, and Fe) in the synthesized Fe-doped TiO_2 nanomaterials were determined by XPS analysis. Figure 5a shows the wide XPS spectrum of the 5% Fe-doped TiO_2 photocatalyst, confirming the presence of Ti, C, Fe, and O elements. Figure 5b shows the XPS spectrum in the Ti 2p region. The peaks indicate that the synthesized titania photocatalyst

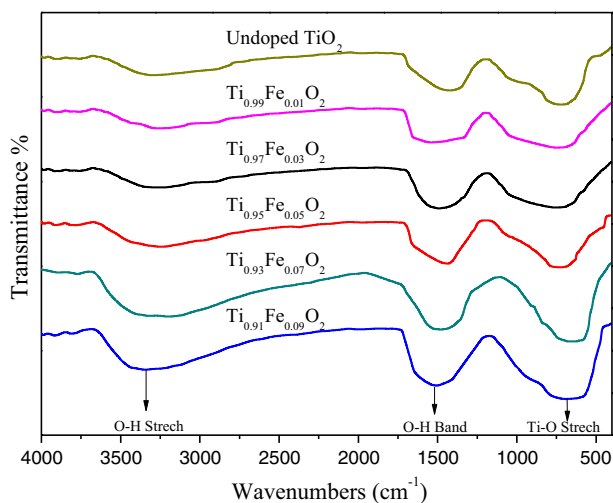


Fig. 4 FTIR spectra of undoped and (1–9%) Fe-doped TiO_2 photocatalysts

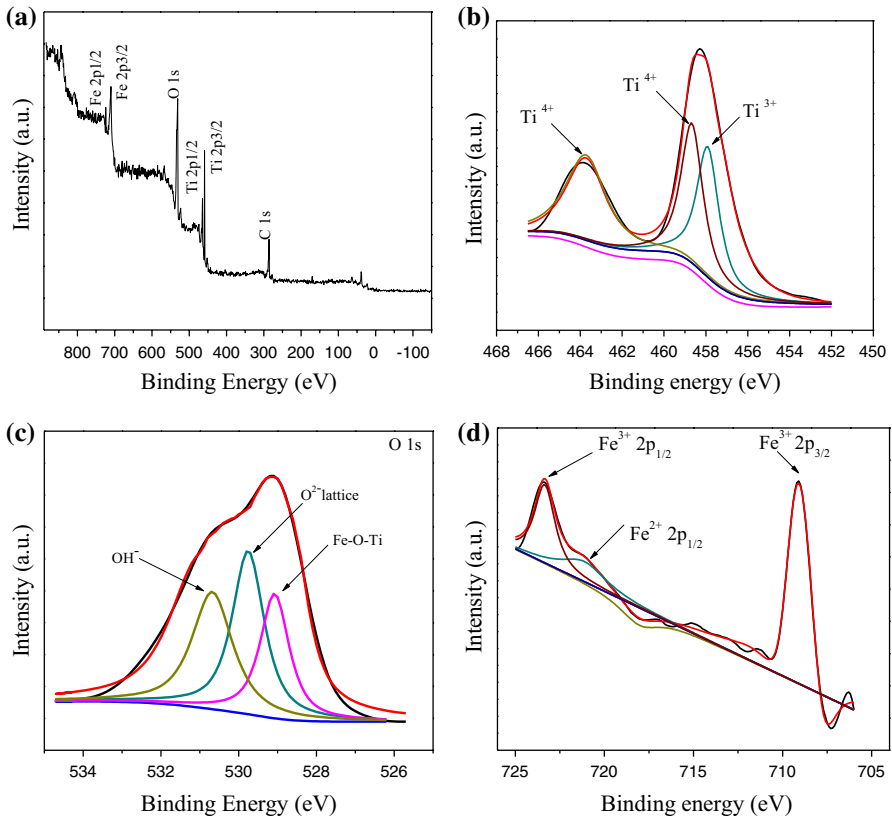


Fig. 5 (a) XPS survey spectrum, and high-resolution scans in (b) Ti 2*p*, (c) O 1*s*, and (d) Fe 2*p* regions for 5% Fe-doped TiO₂ photocatalyst

contained both Ti⁴⁺ and Ti³⁺ oxidation states. The peaks at 458.4 and 463.9 eV indicate the Ti⁴⁺ 2*p*_{3/2} and Ti⁴⁺ 2*p*_{1/2} binding energies, respectively, while the single peak at 457.4 eV indicates the 3+ oxidation state of titanium. Zhang et al. reported approximately the same binding energies for Ti⁴⁺ 2*p*_{3/2} and Ti⁴⁺ 2*p*_{1/2} at 458.5 eV and 464.2 eV, respectively [59]. The spectrum of the synthesized photocatalyst in the O 1*s* region is shown in Fig. 5c, revealing two kinds of O 1*s* peak corresponding to crystal lattice oxygen (O_{lattice}²⁻) in Ti–O–Ti and hydroxyl oxygen (OH⁻) [60]. The main O 1*s* peak (crystal lattice oxygen) at 529.6 eV can be assigned to metallic oxide. The hydroxyl oxygen peak (OH⁻) resulting mainly from chemisorbed water and the peak due to Fe–O–Ti appear at 530.7 eV and 528.9 eV, respectively. Mathews et al. synthesized Fe-doped TiO₂ photocatalyst and reported the crystal lattice oxygen peak at 529.6 eV, hydroxyl oxygen peak at 531 eV, and Fe–O–Ti peak at 529.45 eV, lying in a similar range [61]. Hydroxyl oxygen ions are very reactive and can easily react with other atoms or groups to become stable [42]. Figure 5d shows the Fe 2*p* region of the spectrum for the synthesized photocatalyst, revealing three peaks at 709.4, 723.5, and 721.1 eV; the first two (709.4, 723.5 eV) correspond to

Fe³⁺ while the third (721.1 eV) corresponds to the Fe²⁺ oxidation state of iron. The peaks at 721.1 and 723.5 eV correspond to Fe 2*p*_{1/2}, while that at 709.4 eV corresponds to Fe 2*p*_{3/2}. Hayat et al. [62] found both peaks of Fe³⁺ ions (Fe 2*p*_{1/2} and Fe 2*p*_{3/2}) at 710.9 and 724.9 eV, almost the same values as in the present study. After doping, Fe may exist in the form of Fe(III) and Fe–O–Ti within the TiO₂ lattice [40], which changes the electron density and forms electron–hole traps that result in a change in the electronegativity and enhance the photocatalytic activity of the Fe-doped TiO₂ photocatalysts [40].

Structural morphology

The structural morphology of the undoped and Ti_{0.95}Fe_{0.05}O₂ photocatalysts was investigated by TEM analysis. The TEM and selected-area electron diffraction (SAED) images of the undoped and Ti_{0.95}Fe_{0.05}O₂ photocatalysts are shown in Fig. 6a, both revealing spherical shape. The interplanar spacing (*d*_{hkl}) of some rings was measured from SAED images (Fig. 6a, inset), revealing that both the undoped and Fe-doped TiO₂ were anatase phase, in agreement with the XRD results (JCPDS card no. 21-1272). Particle size histograms for the undoped and Ti_{0.95}Fe_{0.05}O₂ photocatalysts are shown in Fig. 6b, from which average particle sizes of 31.22 ± 7.21 nm and 22.35 ± 5.3 nm, respectively, can be calculated, in good agreement with those calculated using Scherrer's formula in the XRD analysis. The synthesized Fe-doped TiO₂ nanoparticles were spherical in shape with wide particle size range from 20 to 80 nm [63].

EDX analysis was applied to investigate the chemical composition and purity of the synthesized undoped and Fe-doped TiO₂ photocatalysts (Fig. 7). The EDX analysis of the undoped TiO₂ photocatalyst showed only peaks corresponding to Ti and O elements, with no traces of any impurities except carbon (detected due to the carbon tape or adventitious hydrocarbons). Fe peaks were additionally detected along with Ti and O peaks for all the Fe-doped TiO₂ samples. The EDX results are presented in Table 2, confirming the presence of all the elements (Ti, O, and Fe) used in the synthesized Fe-doped TiO₂ photocatalysts.

Mechanism of TiO₂ photocatalyst and enhancement of its activity by Fe doping

Photocatalytic degradation of dye over TiO₂ occurs via photocatalytic oxidation. The detailed mechanism is described in previous works [64–70]. When TiO₂ suspension in water is exposed to radiation with energy greater than its bandgap energy, electrons are generated in the conduction band and holes in the valence band. These photogenerated conduction-band electrons and valence-band holes can reduce and oxidize the dye, respectively. Alternatively, electrons can react with electron acceptors such as O₂ adsorbed on the TiO₂ surface or dissolved in water to form superoxide anion (O₂^{•−}) radicals. Meanwhile, valence-band holes can react with OH[−] or H₂O, oxidizing them to OH[•] radicals, which along with highly oxidizing species (peroxide radicals) are responsible for the photodecomposition of the organic pollutant (dye) molecules. Substitution of Ti⁴⁺ by doping with Fe³⁺ in the TiO₂ lattice

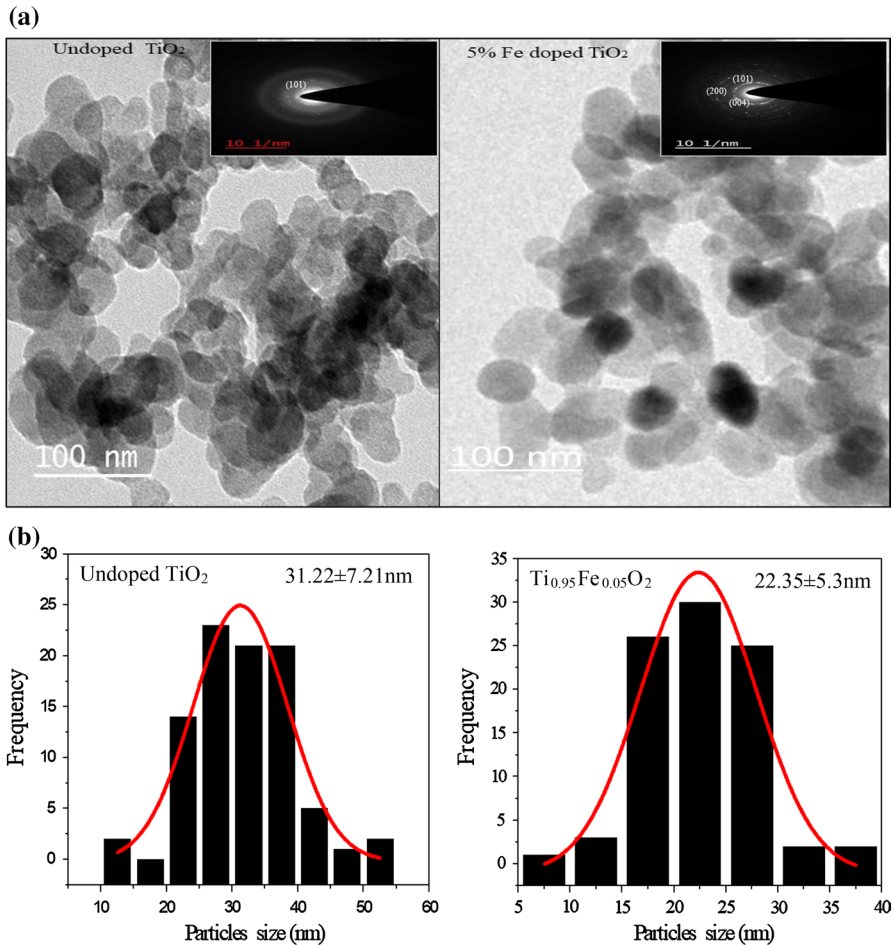


Fig. 6 TEM images of (a) undoped and 5% Fe-doped TiO₂ photocatalysts with inset SAED images, and (b) corresponding size histograms

modifies the band structure, as evidenced by the UV–Vis DRS spectra. The bandgap is narrowed due to the $d-d$ transition between Fe³⁺ and conduction-band electrons and the interaction between Fe³⁺ ions to form Fe⁴⁺ and Fe²⁺, being spread across the bandgap of TiO₂. These Fe⁴⁺ and Fe²⁺ states may trap electrons or holes, which can decrease the recombination rate of electron–hole pairs and hence improve the photocatalytic activity under visible radiation. Fe³⁺ can act as a trap for holes and electrons. Since the Fe³⁺/Fe⁴⁺ energy level lies above the valence band, Fe³⁺ can trap holes ($\text{Fe}^{3+} + \text{h}^+ \rightarrow \text{Fe}^{4+}$). Holes trapped in Fe⁴⁺ can react with OH⁻ to produce hydroxyl radicals ($\text{Fe}^{4+} + \text{OH}^- \rightarrow \text{Fe}^{3+} + \text{OH}^\cdot$). Fe³⁺ can also trap both types of electrons, viz. photogenerated or released from the conduction band, being reduced to Fe²⁺ ($\text{Fe}^{3+} + \text{e}^- \rightarrow \text{Fe}^{2+}$). Fe²⁺ is relatively unstable and hence is oxidized to Fe³⁺ ($\text{Fe}^{2+} \rightarrow \text{Fe}^{3+} + \text{e}^-$). The liberated electron is transferred to an O₂ molecule adsorbed

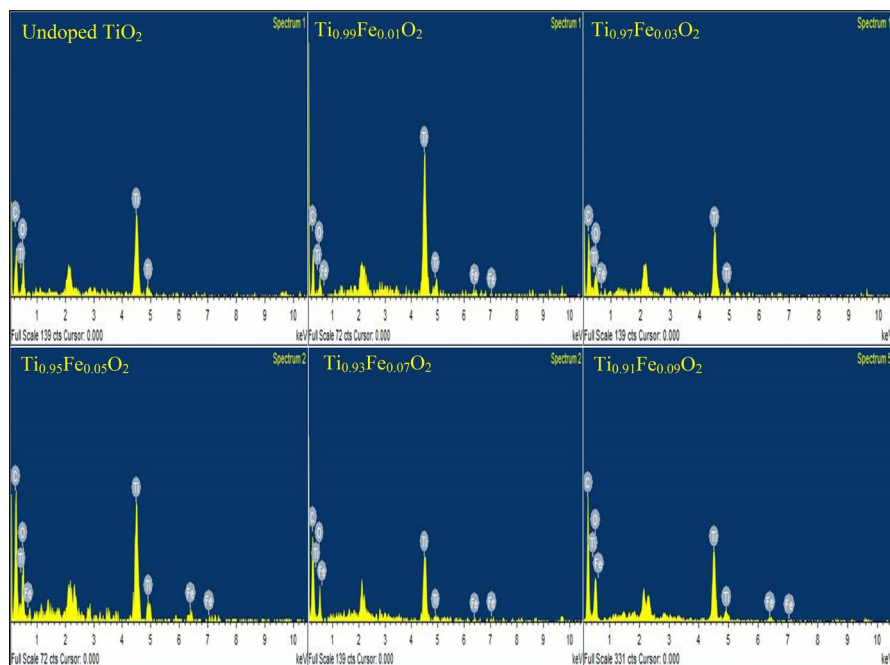


Fig. 7 EDX analysis of undoped and (1–9%) Fe-doped TiO_2 photocatalysts

on the catalyst surface $[\text{O}_{2(\text{ads})} + e^- \rightarrow \text{O}_2^-]$. In this reaction, the O_2^- species has high power to break chemical bonds in the pollutant, while the hydroxyl radicals are powerful oxidizing agents to oxidize organic compounds [71]. O_2^- can easily trap holes and produce hydroxyl ion OH^- and hydroxyl radicals OH^\cdot with water adsorbed on the catalyst surface ($\text{O}_2^- + h^+ \rightarrow \text{O}^-$; $\text{O}^- + \text{H}_2\text{O} \rightarrow \text{OH}^- + \text{OH}^\cdot$). The energy levels of $\text{Fe}^{2+}/\text{Fe}^{3+}$ and $\text{Ti}^{3+}/\text{Ti}^{4+}$ are close, thus the electron liberated by oxidation of Fe^{2+} can be transferred to surface Ti^{4+} , reducing it to Ti^{3+} to react with adsorbed oxygen and produce anion radicals ($\text{Fe}^{2+} + \text{Ti}^{4+} \rightarrow \text{Ti}^{3+} + \text{Fe}^{3+}$; $\text{Ti}^{3+} + \text{O}_2 \rightarrow \text{O}_2^- + \text{Ti}^{4+}$). Also, Fe^{3+} ions at the surface with trapped electron/hole can react directly with an oxygen molecule ($\text{Fe}-\text{O}_2$) or hydroxyl group ($\text{Fe}-\text{OH}$), leading to formation of O_2^- and OH^\cdot radicals, which can also play an important role in photocatalysis [49]. The presence of Ti^{3+} centers and oxygen vacancies [F^+ (shallow trap), F^{+2} (deep traps)] was identified by XPS. Formation of Ti^{3+} ions from Ti^{4+} can take place due to electrons from the conduction band or transferred from oxygen vacancies ($\text{Ti}^{4+} + e^- \rightarrow \text{Ti}^{3+}$). These Ti^{3+} species can interact with surface-adsorbed oxygen, as mentioned above. Oxygen vacancies have the following two functions: (1) trapping of valence-band electrons, or (2) promotion of trapped electrons to the conduction band under visible-light irradiation, thus reducing the recombination phenomenon. In addition, the electron trapped in an oxygen vacancy (F^+ or F^{+2} trap) may also jump to OH acceptor levels to form hydroxyl radicals.

In summary, Fe doping of TiO_2 narrows the bandgap, thus enhancing the adsorption of large numbers of photon with energy between the bandgap of the doped and

Table 2 EDX results for undoped and Fe-doped TiO₂ photocatalysts

Photocatalyst	Element	wt.%	at.%
(a) Pure TiO ₂	C	4.35	10.63
	O	19.51	31.86
	Ti	76.14	57.51
(b) Ti _{0.99} Fe _{0.01} O ₂	C	3.61	8.55
	O	23.43	53.21
	Ti	69.84	35.78
(c) Ti _{0.97} Fe _{0.03} O ₂	Fe	3.12	2.46
	C	5.61	9.34
	O	26.42	45.71
(d) Ti _{0.95} Fe _{0.05} O ₂	Ti	63.10	42.69
	Fe	3.59	2.64
	C	4.22	7.69
(e) Ti _{0.93} Fe _{0.07} O ₂	O	27.51	49.57
	Ti	64.68	40.10
	Fe	4.87	2.26
(f) Ti _{0.91} Fe _{0.09} O ₂	C	3.15	7.44
	O	31.88	55.35
	Ti	59.85	33.57
	Fe	5.12	3.64
	C	4.12	8.25
	O	31.56	52.62
	Ti	57.79	34.50
	Fe	6.53	4.63

undoped material. These charge carriers are trapped at Fe³⁺, Fe²⁺, and Fe⁴⁺ sites as well as Ti³⁺ centers and oxygen vacancies, leading to a significant decrease in the recombination rate of carriers and thereby enhancing the catalytic activity. In this work, the combined effect of these two phenomena, i.e., trapping of electrons and reduction of e⁻/h⁺ recombination, was maximum at 5% Fe doping; hence, the maximum catalytic activity was observed at this concentration.

Kinetic studies of dye degradation

Study of the adsorption of dye on the undoped and Fe-doped TiO₂ photocatalysts showed that only 2–3% of the dye was adsorbed on all the synthesized photocatalysts. Negligible photodegradation of dye was observed in the absence of photocatalyst in the photochemical and open pan reactors.

Kinetic studies were carried out on all 18 systems; one of them (system 10) is presented in Fig. 8. The data obtained from all the systems could be well fit using pseudo-first-order kinetics according to Eq. (3).

$$-\frac{dC}{dt} = K_{app}C, \quad (3)$$

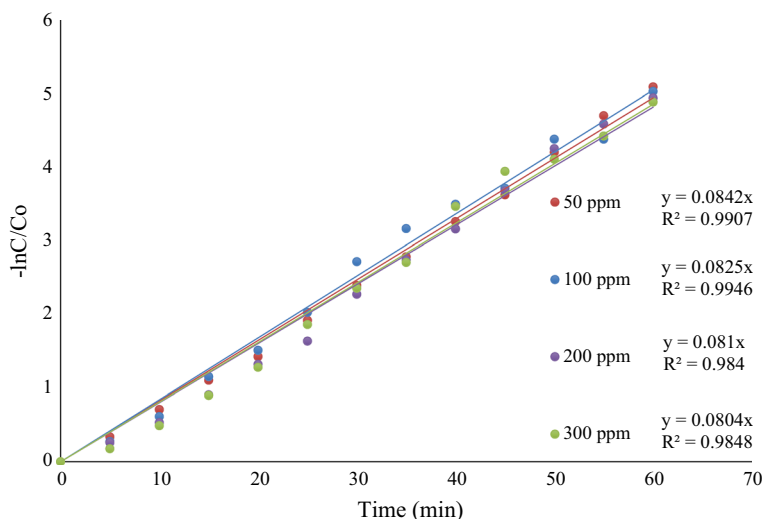


Fig. 8 Kinetic study of degradation of Direct Blue 199 dye in presence of $\text{Ti}_{0.95}\text{Fe}_{0.05}\text{O}_2$ photocatalyst (system 10)

where C is the concentration of the dye solution at time t , C_0 is the the initial concentration of the dye solution, and K_{app} is the apparent first-order rate constant. The value of K_{app} for each system was determined from plots of $-\ln(C/C_0)$ versus t and is presented in Table 3a, b.

From the data obtained in all the kinetic studies, it was observed that the $\text{Ti}_{0.95}\text{Fe}_{0.05}\text{O}_2$ photocatalyst showed the maximum photodegradation ability among all the undoped and Fe-doped TiO_2 photocatalysts (Table 3a, b). The reaction rate constant (K_{app}) of all 18 systems is presented in Table 3a, b. The $\text{Ti}_{0.95}\text{Fe}_{0.05}\text{O}_2$ photocatalyst showed the highest reaction rate constant ($K_{\text{app}} = 8.4 \times 10^{-2} \text{ min}^{-1}$) for 50 ppm dye solution in the photocatalytic reactor with quartz tube. The photocatalytic degradation of different dyes such as Methyl Orange (MO), Rhodamine B (RB), Thymol Blue (TB), Bromocresol Green (BG), and Malachite Green using Fe(III)-doped TiO_2 photocatalysts has been reported, and all followed pseudo-first-order kinetics [34, 72, 73]. The enhancement of the photocatalytic activity was discussed in “[Mechanism of \$\text{TiO}_2\$ photocatalyst and enhancement of its activity by Fe doping](#)” section. It was observed in the present study that, at high doping concentration (7–9% Fe-doped TiO_2), the photodegradation efficiency of the Fe-doped TiO_2 photocatalysts reduced for all 18 systems, indicating that the doping concentration must be optimum. This reduction at high doping concentration can be attributed to multiple trapping of charge carriers and enhanced probability of electron–hole recombination.

Table 3 K_{app} and R^2 values for different systems: (a) 1–9 and (b) 10–18 in the kinetic study of dye photodegradation

Photocatalyst	50 ppm		100 ppm		200 ppm		300 ppm	
	K_{app} (min ⁻¹)	R^2	K_{app} (min ⁻¹)	R^2	K_{app} (min ⁻¹)	R^2	K_{app} (min ⁻¹)	R^2
(a)								
System 1	4.6×10^{-2}	0.989	4.2×10^{-2}	0.989	4.3×10^{-2}	0.979	4.1×10^{-2}	0.968
System 2	5.1×10^{-2}	0.974	5.0×10^{-2}	0.989	5.0×10^{-2}	0.967	4.9×10^{-2}	0.990
System 3	5.9×10^{-2}	0.973	5.5×10^{-2}	0.966	5.5×10^{-2}	0.982	5.4×10^{-2}	0.957
System 4	6.5×10^{-2}	0.951	6.4×10^{-2}	0.965	6.5×10^{-2}	0.952	6.4×10^{-2}	0.952
System 5	4.9×10^{-2}	0.986	4.4×10^{-2}	0.961	4.4×10^{-2}	0.976	4.4×10^{-2}	0.939
System 6	4.2×10^{-2}	0.988	4.2×10^{-2}	0.960	4.1×10^{-2}	0.907	4.0×10^{-2}	0.991
System 7	5.3×10^{-2}	0.993	5.3×10^{-2}	0.992	5.3×10^{-2}	0.990	5.1×10^{-2}	0.984
System 8	6.6×10^{-2}	0.978	6.4×10^{-2}	0.970	6.5×10^{-2}	0.940	6.5×10^{-2}	0.962
System 9	7.3×10^{-2}	0.991	7.3×10^{-2}	0.977	7.1×10^{-2}	0.973	7.2×10^{-2}	0.978
(b)								
System 10	8.4×10^{-2}	0.990	8.2×10^{-2}	0.995	8.1×10^{-2}	0.984	8.0×10^{-2}	0.985
System 11	6.3×10^{-2}	0.988	6.3×10^{-2}	0.976	6.2×10^{-2}	0.984	6.2×10^{-2}	0.976
System 12	5.2×10^{-2}	0.995	5.3×10^{-2}	0.989	5.2×10^{-2}	0.990	5.0×10^{-2}	0.955
System 13	1.1×10^{-2}	0.919	1.0×10^{-2}	0.903	1.0×10^{-2}	0.923	1.0×10^{-2}	0.945
System 14	1.2×10^{-2}	0.930	1.1×10^{-2}	0.929	1.310^{-2}	0.898	1.1×10^{-2}	0.927
System 15	1.5×10^{-2}	0.947	1.4×10^{-2}	0.927	1.2×10^{-2}	0.907	1.1×10^{-2}	0.916
System 16	1.6×10^{-2}	0.959	1.210^{-2}	0.941	1.3×10^{-2}	0.916	1.0×10^{-2}	0.950
System 17	1.1×10^{-2}	0.967	1.0×10^{-2}	0.921	1.0×10^{-2}	0.937	1.1×10^{-2}	0.948
System 18	1.0×10^{-2}	0.964	1.1×10^{-2}	0.915	1.1×10^{-2}	0.926	0.9×10^{-2}	0.947

The photocatalyst without regeneration showed very low activity compared with the regenerated photocatalyst. The photocatalyst without regeneration showed only 6.67% dye degradation ability, which is not significant for photocatalysis applications.

The activity of the regenerated $Ti_{0.95}Fe_{0.05}O_2$ photocatalyst was checked by photodegradation of dye solution (Fig. 9), revealing a decrease in activity with the number of regenerations. Photodegraded and adsorbed Direct Blue 199 dye on the surface of the photocatalyst is the main cause of this decrease in the activity of the photocatalyst, since the dye molecule contains copper in its structure, which can fill pores of the photocatalyst by forming copper oxide (CuO). The observation of a peak at Bragg angle of 35.2° in the XRD pattern of the regenerated photocatalyst confirms the presence of copper (Fig. 10). The XRD peak for copper was found at approximately the same 2θ value for Cu-doped TiO_2 [74, 75].

The photodegradation of Direct Blue 199 dye in the photocatalytic reactor using the best photocatalyst ($Ti_{0.95}Fe_{0.05}O_2$) in the quartz tube (A), the glass tube (B), and the untreated sample (C) are shown in Fig. 11a. Photodegradation of dye using the regenerated $Ti_{0.95}Fe_{0.05}O_2$ photocatalyst in quartz tube is shown

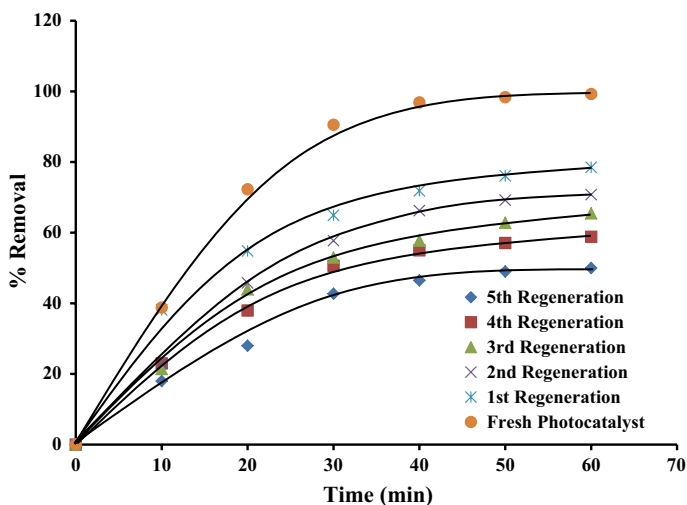


Fig. 9 Performance of fresh and regenerated $\text{Ti}_{0.95}\text{Fe}_{0.05}\text{O}_2$ photocatalyst in photodegradation of Direct Blue 199 dye in the photochemical reactor with quartz tube

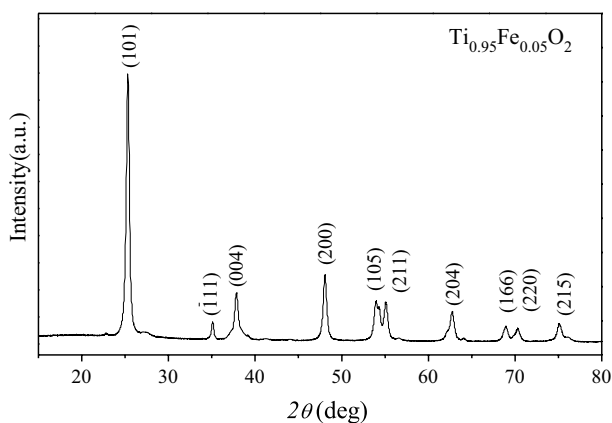


Fig. 10 XRD spectrum of regenerated $\text{Ti}_{0.95}\text{Fe}_{0.05}\text{O}_2$ photocatalyst

in Fig. 11b, where “Rn” indicates the catalyst after n uses. Such regeneration of many photocatalysts including doped TiO_2 [34], TiO_2 composites [54, 76], and graphitic carbon nitride nanosheets [77] has been reported in literature. These photocatalysts have been used to degrade different dyes such as Rhodamine B, Methylene Blue, Methyl Orange, and Crystal Violet.

A comparative study of the prepared undoped TiO_2 and the best among the doped TiO_2 samples, i.e., $\text{Ti}_{0.95}\text{Fe}_{0.05}\text{O}_2$, as well as Aeroxide P-25 was carried out; the results are shown in Fig. 12, revealing that the 5% Fe-doped TiO_2 ($\text{Ti}_{0.95}\text{Fe}_{0.05}\text{O}_2$) photocatalyst showed the best activity .

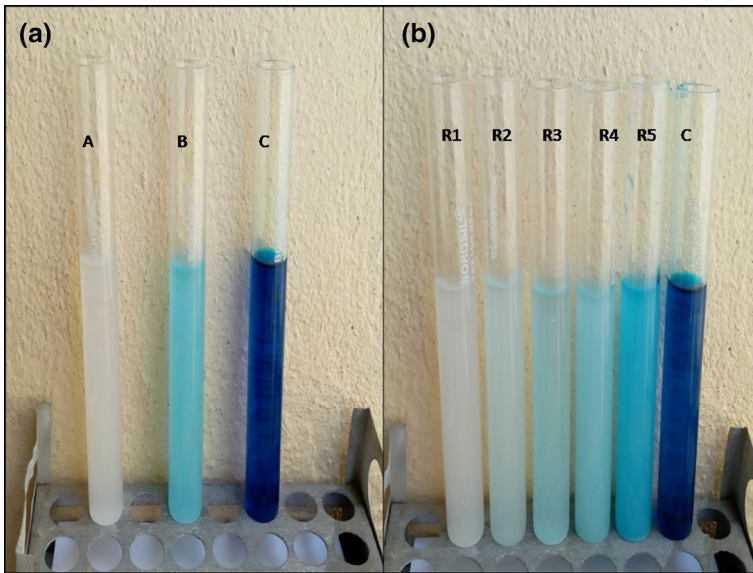


Fig. 11 Photodegradation of Direct Blue 199 dye in photochemical reactor in quartz tube using fresh $Ti_{0.95}Fe_{0.05}O_2$ photocatalyst (a), and regenerated $Ti_{0.95}Fe_{0.05}O_2$ photocatalyst (b)

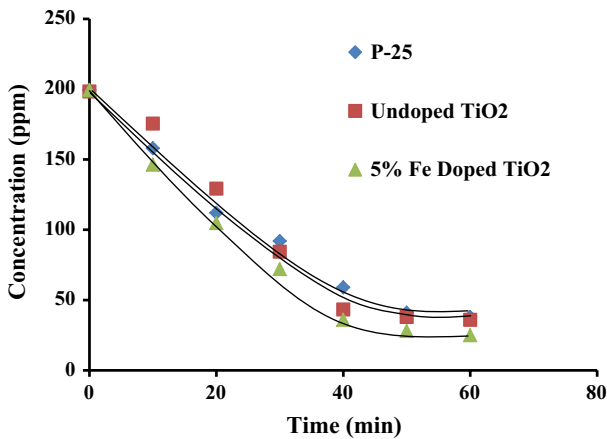


Fig. 12 Comparison of the best photocatalysts among the synthesized undoped TiO_2 , $Ti_{0.95}Fe_{0.05}O_2$, and P-25 for photodegradation of Direct Blue 199 dye

Conclusions

Fe-doped TiO_2 samples with compositions $Ti_{1-x}Fe_xO_2$ ($x=0.00, 0.01, 0.03, 0.05, 0.07, \text{ and } 0.09$) were prepared by a solution combustion method and their photocatalytic activity determined by photodegradation of Direct Blue 199 dye in a photochemical reactor and an open pan reactor under direct sunlight. To enable an

economical photodegradation process, it should be possible to regenerate and reuse the photocatalyst for dye degradation. The results of all 18 systems showed that the $\text{Ti}_{0.95}\text{Fe}_{0.05}\text{O}_2$ photocatalyst exhibited the best photocatalytic activity, measured in terms of dye degradation, among all the synthesized undoped and Fe-doped TiO_2 photocatalysts in both reactors (photochemical and open pan reactor). The photodegradation results for dye solution using regenerated $\text{Ti}_{0.95}\text{Fe}_{0.05}\text{O}_2$ photocatalyst revealed that the activity of the photocatalyst decreased with increasing number of regenerations. The results of this study also show that, with increase in the doping from 1 to 5%, the photocatalyst activity increased, after which it started to decline. The maximum activity was found at 5% doping. A comparison among the synthesized undoped TiO_2 , $\text{Ti}_{0.95}\text{Fe}_{0.05}\text{O}_2$, and commercial Aeroxide P-25 revealed that the synthesized $\text{Ti}_{0.95}\text{Fe}_{0.05}\text{O}_2$ photocatalyst exhibited the highest photocatalytic activity among the three.

Compliance with ethical standards

Conflict of interest There are no conflicts of interest to declare.

References

1. Y.C. Liang, C.C. Wang, C.C. Kei, Y.C. Hsueh, W.H. Cho, T.P. Perng, *J. Phys. Chem. C* **115**, 9498 (2011)
2. L. Chen, F. Chen, Y. Shi, J. Zhang, *J. Phys. Chem. C* **116**, 8579 (2012)
3. M.A. Fox, M.T. Dulay, *Chem. Rev.* **93**, 341 (1993)
4. W.T. Moon, K.S. Lee, Y.K. Jun, H.S. Kim, S.H. Hong, *Sens. Actuators B* **115**, 123 (2006)
5. L. Francioso, D.S. Presicce, A.M. Taurino, R. Rella, P. Siciliano, A. Ficarella, *Sens. Actuators B Chem.* **95**, 66 (2003)
6. L. Zheng, M. Xu, T. Xu, *Sens. Actuators B Chem.* **66**, 28 (2000)
7. A.M. More, J.L. Gunjakar, C.D. Lokhande, *Sens. Actuators B Chem.* **129**, 671 (2008)
8. Y. Liu, X. Wang, F. Yang, X. Yang, *Microporous Mesoporous Mater.* **114**, 431 (2008)
9. P. Evans, D.W. Sheel, *Surf. Coat. Technol.* **201**, 9319 (2007)
10. Y. Paz, Z. Luo, L. Rabenberg, A. Heller, *J. Mater. Res.* **10**, 2842 (2011)
11. R. Fretwell, P. Douglas, *J. Photochem. Photobiol. A Chem.* **143**, 229 (2001)
12. V.P.S. Perera, P.V.V. Jayaweera, P.K.D.D.P. Pitigala, P.K.M. Bandaranayake, G. Hastings, A.G.U. Perera, K. Tennakone, *Synth. Met.* **143**, 283 (2004)
13. Y. Xie, C. Yuan, *J. Mater. Sci.* **40**, 6375 (2005)
14. R.S. Sonawane, B.B. Kale, M.K. Dongare, *Mater. Chem. Phys.* **85**, 52 (2004)
15. C.H. Ao, S.C. Lee, J.C. Yu, *J. Photochem. Photobiol. A Chem.* **156**, 171 (2003)
16. H. Yamashita, M. Harada, J. Misaka, M. Takeuchi, B. Neppolian, M. Anpo, *Catal. Today* **84**, 191 (2003)
17. N. Venkatachalam, M. Palanichamy, V. Murugesan, *Mater. Chem. Phys.* **104**, 454 (2007)
18. H. Yang, K. Zhang, R. Shi, X. Li, X. Dong, Y. Yu, *J. Alloys Compd.* **413**, 302 (2006)
19. H. Lee, M.Y. Song, J. Jurng, Y.-K. Park, *Powder Technol.* **214**, 64 (2011)
20. H. Xie, G. Gao, Z. Tian, N. Bing, L. Wang, *Particuology* **7**, 204 (2009)
21. S. Pavasupree, S. Ngamsinlapasathian, M. Nakajima, Y. Suzuki, S. Yoshikawa, *J. Photochem. Photobiol. A Chem.* **184**, 163 (2006)
22. R. Thapa, S. Maiti, T.H. Rana, U.N. Maiti, K.K. Chattopadhyay, *J. Mol. Catal. A Chem.* **223**, 363 (2012)
23. M.H. Zori, *J. Inorg. Organomet. Polym. Mater.* **21**, 81 (2011)
24. G.L. Li, G.H. Wang, *Nanostruct. Mater.* **11**, 663 (1999)
25. X. Chen, L. Liu, P.Y. Yu, S.S. Mao, *Science* **331**, 746 (2011)
26. C.-Y. Wang, D.W. Bahnemann, J.K. Dohrmann, *Chem. Commun.* **0**, 1539 (2000)

27. W. Zhao, L. Feng, R. Yang, J. Zheng, X. Li, *Appl. Catal. B Environ.* **103**, 181 (2011)
28. Y. Lin, Z. Jiang, X. Hu, X. Zhang, J. Fan, *Appl. Phys. Lett.* **100**, 102105 (2012)
29. M. Zhang, C. Shao, J. Mu, Z. Zhang, Z. Guo, P. Zhang, Y. Liu, *Cryst. Eng. Commun.* **14**, 605 (2012)
30. J. Lin, J. Shen, R. Wang, J. Cui, W. Zhou, P. Hu, D. Liu, H. Liu, J. Wang, R.I. Boughton, Y. Yue, J. Mater. Chem. **21**, 5106 (2011)
31. J. Lu, Q. Han, Z. Wang, *Mater. Res. Bull.* **47**, 1621 (2012)
32. K. Kočí, L. Obalová, Z. Lacný, *Chem. Pap.* **62**, 1 (2008)
33. S. Yu, H.J. Yun, D.M. Lee, J. Yi, *J. Mater. Chem.* **22**, 12629 (2012)
34. R. Fiorenza, M. Bellardita, S. Scirè, L. Palmisano, *Mol. Catal.* **455**, 108 (2018)
35. Y. Li, W.N. Wang, Z. Zhan, M.H. Woo, C.Y. Wu, P. Biswas, *Appl. Catal. B Environ.* **100**, 386 (2010)
36. S. Rengaraj, X.Z. Li, *J. Mol. Catal. A Chem.* **243**, 60 (2006)
37. N.-L. Wu, M.-S. Lee, *Int. J. Hydrog. Energy* **29**, 1601 (2004)
38. K. Kočí, K. Matějů, L. Obalová, S. Krejčíková, Z. Lacný, D. Plachá, L. Čapek, A. Hospodková, O. Šolcová, *Appl. Catal. B Environ.* **96**, 239 (2010)
39. T. Ali, P. Tripathi, A. Ameer, R. Waseem, S.A. Arham, A. Ateeq, M. Muneer, *Mater. Res. Exp.* **4**, 015022 (2017)
40. W.C. Hung, Y.C. Chen, H. Chu, T.K. Tseng, *Appl. Surf. Sci.* **255**, 2205 (2008)
41. W. Raza, M.M. Haque, M. Muneer, M. Fleisch, A. Hakkı, D. Bahnemann, *J. Alloys Compd.* **632**, 837 (2015)
42. B. Xin, L. Jing, Z. Ren, B. Wang, H. Fu, *J. Phys. Chem. B* **109**, 2805 (2005)
43. L. Singh, U.S. Rai, K.D. Mandal, N.B. Singh, *Prog. Cryst. Growth Charact. Mater.* **60**, 15 (2014)
44. L. Madhvi, L. Singh, S. Saroj, Y. Lee, S.V. Singh, *J. Mater. Sci. Mater. Electron.* **27**, 2581 (2016)
45. C.L.J. Bodson, S.L. Pirard, R. Pirard, L. Tasseroul, C. Bied, M.W.C. Man, B.T. Heinrichs, S.P.D. Lambert, *J. Mater. Sci. Chem. Eng.* **8**, 16 (2014)
46. N. Nasralla, M. Yeganeh, Y. Astuti, S. Piticharoenphun, N. Shahtahmasebi, A. Kompany, M. Karimipour, B.G. Mendis, N.R.J. Poolton, L. Šiller, *Sci. Iran* **20**, 1018 (2013)
47. B. Choudhury, R. Verma, A. Choudhury, *RSC Adv.* **4**, 29314 (2014)
48. Z. Li, W. Shen, W. He, X. Zu, *J. Hazard. Mater.* **155**, 590 (2008)
49. L. Wen, B. Liu, X. Zhao, K. Nakata, T. Murakami, A. Fujishima, *Int. J. Photoenergy* **10**, 368750 (2012)
50. J. Yu, J.C. Yu, X. Zhao, *J. Sol-Gel Sci. Technol.* **24**, 95 (2002)
51. M. Anpo, Y. Ichihashi, M. Takeuchi, H. Yamashita, *Stud. Surf. Sci. Catal.* **46**, 305 (1999)
52. M. Anpo, Y. Ichihashi, M. Takeuchi, H. Yamashita, *Res. Chem. Intermed.* **24**, 143 (1998)
53. M. Anpo, *Catal. Surv. Jpn.* **1**, 169 (1997)
54. S. Bougarrani, K. Skadell, R. Arndt, M. El Azzouzi, R. Gläser, *J. Environ. Chem. Eng.* **6**, 1934 (2018)
55. C.L. Luu, Q.T. Nguyen, S.T. Ho, *Adv. Nat. Sci. Nanosci. Nanotechnol.* **1**, 015008 (2010)
56. K. Nagaveni, M.S. Hegde, G. Madras, *J. Phys. Chem. B* **108**, 20204 (2004)
57. T. Lopez, J.A. Moreno, R. Gomez, X. Bokhimi, J.A. Wang, H. Yee-Madeira, G. Pecchi, P. Reyes, *J. Mater. Chem.* **12**, 714 (2002)
58. B.M. Reddy, I. Ganesh, E.P. Reddy, A. Fernández, P.G. Smirniotis, *J. Phys. Chem. B* **105**, 6227 (2001)
59. Q. Zhang, Y. Li, E.A. Ackerman, M. Gajdardziska-Josifovska, H. Li, *Appl. Catal. A Gen.* **400**, 195 (2011)
60. C. Ren, W. Qiu, Y. Chen, *Sep. Purif. Technol.* **107**, 264 (2013)
61. N.R. Mathews, M.A. Cortes Jacome, C. Angeles-Chavez, J.A.T. Antonio, *J. Mater. Sci. Mater. Electron.* **26**, 5574 (2015)
62. H. Khan, I.K. Swati, *Ind. Eng. Chem. Res.* **55**, 6619 (2016)
63. D. Singh, P. Yadav, N. Singh, C. Kant, M. Kumar, S.D. Sharma, K.K. Saini, *J. Exp. Nanosci.* **8**, 171 (2013)
64. A. Houas, H. Lachheb, M. Ksibi, E. Elaloui, C. Guillard, J.-M. Herrmann, *Appl. Catal. B Environ.* **31**, 145 (2001)
65. A. Bianco Prevot, C. Baiocchi, M.C. Brussino, E. Pramauro, P. Savarino, V. Augugliaro, G. Marci, L. Palmisano, *Environ. Sci. Technol.* **35**, 971 (2001)
66. K. Tanaka, K. Padermpole, T. Hisanaga, *Water Res.* **34**, 327 (2000)
67. C. Galindo, P. Jacques, A. Kalt, *J. Photochem. Photobiol. A Chem.* **130**, 35 (2000)

68. H. Zhan, H. Tian, *Dyes Pigm.* **37**, 231 (1998)
69. J. Bandara, J.A. Mielczarski, J. Kiwi, *Langmuir* **15**, 7680 (1999)
70. N. Daneshvar, D. Salari, A.R. Khataee, *J. Photochem. Photobiol. A Chem.* **157**, 111 (2003)
71. H. Moradi, A. Eshaghi, S.R. Hosseini, K. Ghani, *Ultrason. Sonochem.* **32**, 314 (2016)
72. T.K. Ghorai, S.K. Biswas, P. Pramanik, *Appl. Surf. Sci.* **254**, 7498 (2008)
73. M. Asiltürk, F. Sayılkan, E. Arpaç, *J. Photochem. Photobiol. A Chem.* **203**, 64 (2009)
74. X.J. Yang, S. Wang, H.M. Sun, X.B. Wang, J.S. Lian, *Trans. Nonferrous Met. Soc. China* **25**, 504 (2015)
75. M. Sahu, P. Biswas, *Nanoscale Res. Lett.* **6**, 441 (2011)
76. A. Meng, J. Xing, W. Guo, Z. Li, X. Wang, *J. Mater. Sci.* **53**, 14328 (2018)
77. A. Akhundi, A. Habibi-Yangjeh, *J. Colloid Interface Sci.* **504**, 697 (2017)